Phys Chem Minerals (1992) 19:25–38

PHYSICS AND CHEMISTRY OF MINERALS

Structure of the $\alpha Fe_xAl_{1-x}OOH$ Solid Solution

I. Evidence by Polarized EXAFS for an Epitaxial Growth of Hematite-Like Clusters in Fe-Diaspore

J.L. Hazemann[1,2], **A. Manceau**[2], **Ph. Sainctavit**[2], **and C. Malgrange**[2]

[1] Centre de Géochimie de la Surface, CNRS UPR6251, 1 rue Blessig, F-67084 Strasbourg, France
[2] Laboratoire de Minéralogie-Cristallographie, Universités Paris 6 et 7 et CNRS UA09, Tour 16, 4 place Jussieu, F-75252 Paris, France

Received January 25, 1991 / Accepted January 2, 1992

Abstract. The three-dimensional local organisation around Fe atoms in a natural diaspore ($\alpha Al_{0.9955}Fe_{0.0045}OOH$) has been investigated by angular measurements of X-ray absorption spectra. It is demonstrated that in a single crystal of diaspore, the absorption cross-section exhibits the special case of trichroism where three independent measurements are needed to determine the absorption cross-section for any direction of polarization. Extended X-ray absorption fine structure (EXAFS) spectra were thus recorded at the following orientations of the polarization vector: $\underline{\varepsilon} \parallel [100]$, $\underline{\varepsilon} \parallel [010]$, and $\underline{\varepsilon} \parallel [001]$. The incoming white beam was monochromatized using two Si(331) crystals, which deliver at the Fe K-edge a completely linearly polarized X-ray beam. The reliability of our measurements was checked by comparing the isotropic EXAFS spectrum calculated from the three orthogonal measurements to the one of the diaspore powder recorded at the magic angle. It is shown that Fe^{3+} ions are not randomly distributed within the diaspore framework. Furthermore, only part of the Fe^{3+} ions substitutes Al, the others being located in the channels of the structure. The 3D local structure of the Fe domains has been modeled assuming hematite-like clusters of three Fe octahedra topotactically grafted to aluminous chains. These Fe clusters are thought to represent ancient multinuclear Fe surface complexes having formed at the time of the diaspore growth, and being sealed in its bulk structure. The whole crystal of diaspore is then thought to have kept the memory of the heterogeneous nucleation mechanism of these hematite nuclei. In addition to the well-known examples of atom segregations, ion vacancies, and intergrowths of discrete phases, this new type of crystal defect represents another evidence of non-equilibrium crystallization process under the thermodynamic and kinetic conditions that prevail at the earth's surface.

Introduction

Iron and aluminium are among the most abundant cations at the earth's surface. Because of the identity of their charges, and similarity of their ionic radii, Fe^{3+} and Al^{3+} are encountered together in a large variety of phyllosilicates and oxides. However, in the case of isomorphic substitutions the slight differences of their ionic radii (0.65 Å and 0.53Å, respectively) cause variations in unit cell parameters and structural disorders at high substitution rate (Thiel 1963; Schulze 1984; Schulze and Schwertmann 1984, 1987). No oxide builds a complete solid solution over the whole $Fe^{3+}-Al^{3+}$ range. For instance the $\alpha Fe_{1-x}Al_xOOH$ solid solution unmixes for $0.33<x<0.85$. The present Polarized EXAFS (P-EXAFS) investigation was undertaken to analyse, at the local scale, the substitution mechanism of Fe for Al in a single crystal of diaspore. This first report is part of an extended structural work realized onto natural and synthetic α(Fe, Al)OOH oxides, which aims at understanding how the process of unmixing takes place at both medium and short range order.

Our knowledge of the crystal chemical behaviour of trace elements is extremely limited because very few structural techniques are sensitive to trace element incorporation. For several years, EXAFS spectroscopy has become one of these inasmuch as it is capable of assessing the localisation and distribution of diluted cations in minerals. Recent EXAFS studies have shown that the actual structure of minerals at the 2–5 Å scale often differs from the average structure derived from diffraction-based techniques. More specifically, these studies have established that minerals formed at the earth's surface, i.e. at low temperature, most often possess a heterogeneous structure on a very fine scale. Two types of structural situations have yet been identified. *(i)* A simple deviation from the random distribution of atoms in a series of solid-solutions (Manceau 1990). The non-random distribution of atoms in low-temperature materials seems to be the rule rather than the exception. *(ii)* Existence of a discrete phase intimately mixed with the major one. These two phases can either exhibit no structural relationships, e.g. (Co, Ni)-asbolane and Ni-asbolane (Chuchrov et al. 1980, 1987; Manceau et al. 1987) or be intergrown, e.g. Fe-containing vernadite and Mn-containing goethite (Manceau and Combes 1988; Manceau et al. 1992). This paper reports a new example belonging to this latter class of heterogeneity. It is shown that, in a single crystal of Fe^{3+}-containing diaspore (0.45 mole %), $Fe(O, OH)_6$-octahedra arrange like in an hematite structure, these hematite-like clusters being epitaxially grown towards the channels of diaspore.

The cationic environment around Fe atoms has been probed by P-EXAFS. When emitted in a bending magnet, the synchrotron beam is linearly perfectly polarized only in the plane of the electron/positron orbit, while radiation above and below this plane is elliptically polarized. A very high linear polarization rate has been obtained by a nearly 45° Bragg angle monochromator described below in the second part of "theoretical consideration". In the classical plane-wave approximation, the angular dependence of the EXAFS term χ has been determined by Teo and Lee (1979) and Stern and Heald (1983), and can be written in the following way

$$\chi(k, \theta) = \sum_{j} \sum_{i=1}^{\underline{N}_j} 3 \cos^2 (\underline{\theta}_j^i) \cdot \chi_{iso}^j(k) \tag{1}$$

where the index j runs over all the shells around the absorbing atom, the index i runs over all the $\underline{N}_j$ atoms of the j shell, $\underline{\theta}_j^i$ is the angle between the polarization vector $\underset{\sim}{\varepsilon}$ and the vector $\underline{r}_j^i$ that binds the absorbing atom to the i^th^ atom of the j^th^ shell, and χ_{iso} holds for the powder. Different from the isotropic EXAFS, which yields a one-dimensional map of the local structure about the target atom, by rotating a single crystal into the X-ray beam, a three-dimensional map can be constructed. Furthermore, when $\underset{\sim}{\varepsilon}$ points to a given scatterer, its wave amplitude is three-times enhanced. Thus, angular measurements give access to directional structural and chemical information, and permits to detect and filtrate weak atomic shells contribution, which would be unperceived when analysing powder spectra. Given the low symmetry and multielement composition of most minerals, P-EXAFS allows to make inroads towards a much more satisfying analysis of their local structure.

At present only few mineralogical applications of EXAFS have taken advantage of possibilities offered by angular measurements. Two major applications have so far been achieved, but others, like the measurement of a sample texture, are in progress. The first straightforward application has consisted to select the EXAFS contribution of a chosen atomic-pair. Such an atomic-pair selectivity is particularly interesting each time different atomic-pairs are located at about the same distance from the X-ray absorber, since, in a powder experiment, the Fourier transform does not permit to filter each of these atomic-pair contribution (Manceau and Decarreau 1988). For instance, the separation by P-EXAFS of the three elementary Fe-(Fe, Mg, Si) contributions in the phlogopite-annite series has permitted, for the first time, to quantitatively compare EXAFS and NMR results onto the atomic environments of cations in minerals (Manceau et al. 1988, 1990; Manceau 1990). Waychunas and Brown (1990) have also used this technique to differentiate between the contributions of two oxygen subshells in the distorted Fe^{3+} site of epidote. A second kind of application of P-EXAFS in mineralogy consists in the determination of the site occupancy of an atom. In chlorite this technique has permitted to determine the percentage of Fe atoms located in the brucitic and in the micaceous layers (Manceau et al. 1988). When applied to chain framework, P-EXAFS enables us to look at the site location and distribution of atoms within and between chains. Furthermore in the case of multiple octahedral chains, like in diaspore, it is even possible to separate contributions of nearest cations along the single-chain the X-ray absorber belongs to, from those of cations located in the adjacent single-chain. Keeping in mind the aforementioned enhancement in the accuracy of structural data in a P-experiment, such an "EXAFS-chaining" experiment is attempted to provide a reliable three-dimensional description of the local environment around the X-ray absorber, and hence, in the case of clusters, of their 3D structure. This technique is more especially interesting in the case of trace elements since such an advanced description of their local structure is not accessible by any other method. This new application of EXAFS spectroscopy will permit us to shed direct light on the structure of the "real crystal", as opposed to that of the "virtual crystal", which is determined by diffraction techniques. In a certain sense, EXAFS-chaining experiments can be compared with ALCHEMI (atom location by channelling-enhanced micro analysis, Tafto and Buseck 1983). In this transmission electron microscopy (TEM-) based method the site location of diluted elements along channels of chain-minerals can be identified owing to channelling effects in the inelastic scattering of fast electrons.

Theoretical considerations

Angular Dependence of X-ray Absorption Spectroscopy (XAS) Measurements in α(Fe, Al)OOH

The absorption cross-section is invariant under the operations of the crystal space group but this trivial result is not so evident. Indeed the description of inner level spectroscopy is commonly based on a local theory where an atom absorbs a photon and ejects a photoelectron. In X-ray absorption, the core-hole left by the photoelectron breaks the translational symmetry of the crystal and we are left with a process whose only symmetry is the local point group of the absorbing atom. Since it is impossible to distinguish between the different possible absorbing centers we have to average the cross section for a specific atom over all the atoms of the unit cell. It is this average that gives to the experimental cross-section the symmetry of the full point group of the crystal space group.

α(Fe, Al)OOH belongs to the space group D_{2h}^{16} (Pnma); the full point-group is D_{2h}(mmm). For this class of crystal it has been shown that the absorption cross-section in the dipolar approximation exhibits the special case of trichroism where three independent parameters are needed to determine the absorption cross-section for any direction of polarization (Brouder 1990). The local point-group for the site of iron in α(Fe, Al)OOH is C_s(m).

For $C_s(m)$ the dependence of the absorption cross-section is also trichroic but with four independent parameters. Wer are going to show that it is indeed the case, pointing out clearly which parameters are zero because of the local site of iron and which are non-zero but cannot be determined experimentally due to the full point-group of the crystal.

The dipole absorption cross-section can be described by the Golden Rule. For a photon of energy $h\nu$, it reads:

$$\sigma(\nu)=4\pi^2\alpha h\nu\sum_{i,f}|\langle f|H_{int}|i\rangle|^2\delta(E_f-E_i-h\nu) \qquad (2)$$

where α is the fine structure constant. The δ function insures the conservation of energy. $|i\rangle$ and $|f\rangle$ are the electronic wave functions of the initial and final states and H_{int} is the interaction Hamiltonian. The first simplification is to set in the dipolar approximation that is relevant when the spatial extent of the initial state is negligeable compare to the wavelength of the photon. It is verified for K-edges of elements lighter than silver (Müller et al. 1984). In the dipolar approximation the interaction Hamiltonian is simply expressed $H_{int}=\vec{\varepsilon}\cdot\vec{r}$ where ε is the normalized polarization vector of the photon and r is the variable of integration.

There is no complete description of the relations between symmetry and absorption. Some recent papers are even confusing since their incompleteness is not mentioned (Vvedinski et al. 1987). On the other hand Brouder gave a complete description for the case of linear polarization in the dipolar and quadrupolar approximations and Goodkoep (1989) presented a large description of the absorption of circularly polarized light in an atomic spherical potential. However the theory of absorption of elliptically polarized light in any point group symmetry remains to be done. In the following part we intend to present an example of how to handle the angular dependence of X-ray absorption in the simple case of linear polarization. Since it is the first time to our knowledge that monoclinic and orthorhombic symmetries are involved in an experimental work on X-ray absorption we have somewhat emphasized the details of the calculations.

In any orthonormal referential $R(x, y, z)$ where

$$\vec{\varepsilon}=\varepsilon_1\vec{x}+\varepsilon_2\vec{y}+\varepsilon_3\vec{z} \quad \text{and} \quad \vec{r}=r_1\vec{x}+r_2\vec{y}+r_3\vec{z}$$

The dipolar cross-section can be expressed as

$$\sigma(\nu)=4\pi^2\alpha h\nu\sum_f\left|\left\langle f\left|\sum_{j=1}^{3}\varepsilon_j r_j\right|i\right\rangle\right|^2\delta(E_f-E_i-h\nu)$$
$$=\sum\varepsilon_j\varepsilon_k\sigma_{jk} \qquad (3)$$

In symmetries lower than orthorhombic, it is obvious that there is no need to determine the base where (σ_{jk}) is diagonal since this base is a complicated function of the photon energy. When the symmetry is higher than orthorhombic, (σ_{jk}) is obviously diagonal in the higher symmetry axes. Nonetheless it is to be noted that the construction of the indicatrix that is common for optics is of very little use for X-rays, because here we are dealing with absorbing materials and in the short wavelength region the behaviour of the refractive index is much different from the case of long wavelength. In the X-ray region the refractive index is complex and can be expressed in the way $\tilde{n}=1-\delta+i\beta$, where $1\gg\delta\gg\beta$ (for instance $\delta\approx10^{-5}$ and $\beta\approx10^{-7}$ for a borosilicale glass at 6 keV) [Paratt 1954]. The indicatrix is to a good approximation a sphere of radius 1. Even in uniaxial or biaxial crystals there is only one propagating beam whatever the polarization might be. So the usual problems that are addressed in optical birefringence (direction of propagation, wave velocity) are not relevant for X-rays in crystals.

The Monocrystal Case

We consider the case of the orthonormal referential $R(e_1, e_2, e_3)$ the axes of which are parallel to the symmetry axes (a, b, c). We first calculate the cross-section at one site of iron, labelled Fe_0. The local point-group of iron site is $C_s(m)$. That means that the crystal is invariant under the plane symmetry m passing by the absorbing iron atom and perpendicular to the b axis (e_2 direction in the R referential). This symmetry implies that for any energy $\sigma_{12}=\sigma_{23}=0$ and that the cross-section at this specific iron site can be written as

$$\sigma_{FeO}(\vec{\varepsilon})=\varepsilon_1^2\cdot\sigma_{11}+\varepsilon_2^2\cdot\sigma_{22}+\varepsilon_3^2\cdot\sigma_{33}+2\varepsilon_1\varepsilon_3\cdot\sigma_{13} \qquad (4)$$

However in α(Fe, Al)OOH there are four cation sites in the unit cell which means that the experimental cross section is an average on the four sites of the unit cell. For the average one has to calculate the absorption cross section at any specific iron site. It can be done by rotating the reference frame R while the polarization is kept constant in the laboratory. This operation is equivalent to a rotation of the polarization vector while not changing the crystal. In doing so the terms σ_{jk} for the different iron sites are obviously the same while the expression, equivalent to (4), that relates the cross-section of each individual iron site to (σ_{jk}) is modified. It can be easily shown that the crossed term σ_{13} cancel in the average. The average over the unit cell leads to the total absorption cross-section

$$\sigma(\vec{\varepsilon})=\varepsilon_1^2\cdot\sigma_{11}+\varepsilon_2^2\cdot\sigma_{22}+\varepsilon_3^2\cdot\sigma_{33} \qquad (5)$$

The trichroism class of D_{2h} is indeed the three independent parameter class. The parameter σ_{13} cannot be measured by the experiment because it disappears from the cross-section due to the crystal full symmetry but it is worth noticing that σ_{13} is non-zero and can be extracted from a cluster calculation. This comes from the fact the X-ray absorption process is essentially a local phenomenon due to the localization of the initial state. Equation (5) holds for the whole X-ray absorption spectrum; no approximations are made except for the dipolar approximation; the choice of the referential $R(e_1, e_2, e_3)$ with its axes parallel to (a, b, c) is of course essential.

The Powder Case

A powder is an ensemble of monocrystals that have random orientations in the referential of the laboratory. For any of the monocrystals the cross-section can be expressed by (4).

$$\sigma^{p}(\vec{\varepsilon})=\sum_{j,k}\varepsilon_j\,\varepsilon_k\,\sigma^{p}_{jk}$$

where p refers to the p^th monocrystal. The total cross-section is the average of the $\underline{\sigma}_p$ over all the monocrystals, which is equivalent to an average over all the directions of the polarization vector. It then comes that

$$\sigma_{iso}=\tfrac{1}{3}(\sigma_{xx}+\sigma_{yy}+\sigma_{zz}) \tag{6}$$

since

$$\frac{1}{4\pi}\int_{\Omega}d\Omega(\varepsilon_1\,\varepsilon_j)=\tfrac{1}{3}\delta_{ij}$$

where δ_{ij} is the Kronecker delta.

Since the trace of a matrix is invariant under any unitary transformation, Equation (6) holds for any referential R. From (6) it can be deduced that for a monocrystal with any structure, the average among the spectra measured for three orthogonal directions of polarization gives the isotropic spectrum.

Application to EXAFS Formula

The angular dependence of the EXAFS formula is given by (2). In a given referential $R(\underset{\sim}{x}, \underset{\sim}{y}, \underset{\sim}{z})$ with $\underset{\sim}{\varepsilon}$ the polarization vector and $\underset{\sim}{r}^{i}_{j}$ the position vector of the i^th atom of the j^th shell given by

$$\vec{\varepsilon}=\varepsilon_1\,\vec{x}+\varepsilon_2\,\vec{y}+\varepsilon_3\,\vec{z} \quad \text{and} \quad \vec{r}^{\,i}_{j}=r^{i}_{j}(x^{i}_{j}\,\vec{x}+y^{i}_{j}\,\vec{y}+z^{i}_{j}\,\vec{z})$$

$\chi(k, \theta)$ can be written

$$\chi(k,\theta)=\varepsilon_x^2\,\chi_{xx}+\varepsilon_y^2\,\chi_{yy}+\varepsilon_z^2\,\chi_{zz}+2\varepsilon_x\cdot\varepsilon_y\,\chi_{xy} +2\varepsilon_x\cdot\varepsilon_z\,\chi_{xz}+2\varepsilon_y\cdot\varepsilon_z\,\chi_{yz} \tag{7}$$

with

$$\chi_{pq}=\sum_{j}\chi^{j}{}_{iso}(k)\sum_{i=1}^{N_i}3p^{i}_{j}\cdot q^{i}_{j}$$

for p and q equal to x, y or z.

The angular dependence of $\underline{\chi}$ in (7) is obviously the same as for the total absorption cross-section in (2). The conclusions to which we arrived for the general case of the whole X-ray absorption spectrum stand also for the EXAFS region. In the referential $R(\underset{\sim}{e}_1, \underset{\sim}{e}_2, \underset{\sim}{e}_3)$ with axes parallel to $(\underset{\sim}{a}, \underset{\sim}{b}, \underset{\sim}{c})$, it follows from (5) that $\underline{\chi}$ can be written as

$$\chi(k,\theta)=\varepsilon_1^2\,\chi_{11}+\varepsilon_2^2\,\chi_{22}+\varepsilon_3^2\,\chi_{33}$$

and from (6) that

$$\chi_{iso}(k,\theta)=\tfrac{1}{3}(\chi_{11}+\chi_{22}+\chi_{33}) \tag{8}$$

Polarization Rate

If we want to have a veritable directional probe and to well separate any contribution, the polarization rate should be compelled near to 100%. In order to obtain an X-ray beam linearly polarized with a high rate of polarization, we have used a well-collimated beam to take benefit of the polarization of the synchrotron beam, and then a monochromator with a Bragg angle close to 45° in order to still improve the polarization rate.

Polarization of the Synchrotron Beam Emitted by a Bending Magnet

Whatever the wavelength, the beam is linearly polarized in the horizontal orbit plane, and elliptically polarized out of this plane (Fig. 1). Figure 2 gives the relative inten-

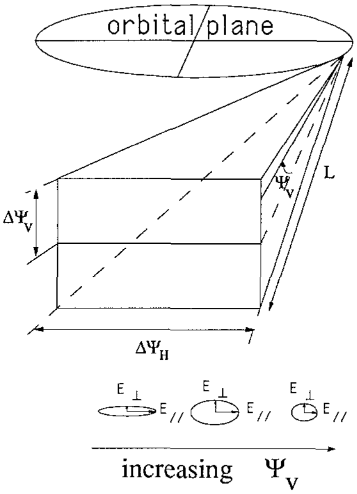

Fig. 1. Geometrical characteristics of the synchrotron beam. $\underline{\Psi}_v$: vertical emission angle, $\underline{\Delta\Psi}_v$ and $\underline{\Delta\Psi}_H$: beam acceptances in the vertical and horizontal planes, respectively. $\underset{\sim}{L}$ is the distance from the optical source. At the bottom are represented some states of polarization for increasing values of $\underline{\Psi}_v$. The scale between the orbital plane and the X-ray beam is not respected

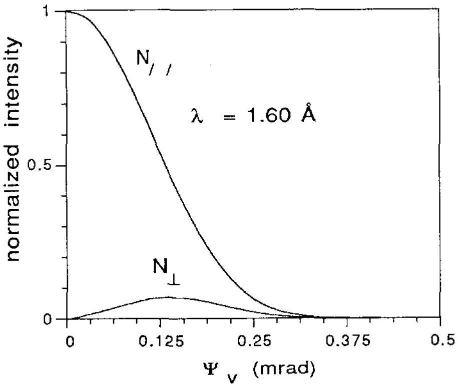

Fig. 2. Normalized intensities of horizontal ($N_{\parallel}$) and vertical ($N_\perp$) polarization components as a function of $\underline{\Psi}_v$ and for $\underline{\lambda}$ = 1.60 Å on the DCI storage ring working at 1.85 Gev ($\underline{\lambda}_c$ = 3.4 Å) (emission from a bending magnet)

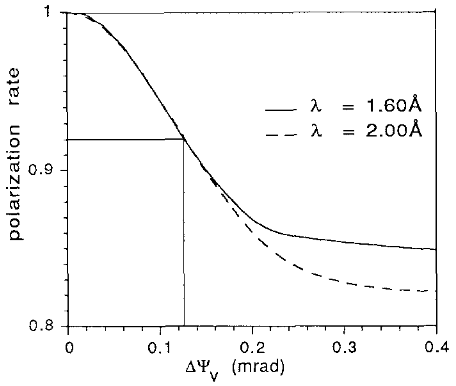

Fig. 3. Linear polarization rate P_l as a function of the vertical half-divergence ($\Delta\Psi_v$) of the incident beam at $\lambda = 1.60$ Å and $\lambda = 2.00$ Å

sities at $\lambda = 1.60$ Å of the components parallel ($N_\parallel$) and perpendicular ($N_\perp$) to the orbit plane as a function of the emission angle Ψ_v defined in Fig. 1. The polarization rate P_l of the beam is defined by

$$P_l = \frac{N_\parallel - N_\perp}{N_\parallel + N_\perp} = \frac{1 - \tau_1}{1 + \tau_1} \tag{9}$$

where

$$\tau_1 = \frac{N_\perp}{N_\parallel}$$

In Fig. 3, P is plotted as a function of the half-vertical divergence $\Delta\Psi_v$ of the beam. We can see that the polarization rate is very close to 100% for a vertical half-divergence $\Delta\Psi_v \leq 0.02$ mrad (F. Wuilleumier 1973). In our experiment, the size of the vertical source (σ_z) was equal to 2 mm, and the incident beam was vertically delimited by a slit with 3 mm width and located at 20 m from the source. The half-vertical divergence of the incident beam can be considered as being equal to $\Delta\Psi_v = 0.125$ mrad, which corresponds to a polarization rate of 92% at the Fe K-edge ($\lambda = 1.74$ Å).

Polarization by the Bragg Reflections: Case of Perfect Crystals Without Absorption

Let us now consider the polarization rate which results from two Bragg reflections. For perfect crystals, the X-ray dynamical theory applies. Figure 4 shows the theoretical reflecting power after two reflections for the two polarizations, respectively perpendicular (σ-polarization) and parallel (π-polarization) to the diffraction plane (plane formed by the incident and diffracted beams). The width ω of the domain of total reflection depends on the polarization and is given in a symmetrical case by (Zachariasen 1945):

$$\omega = |C| \, \omega_D \tag{10}$$

where

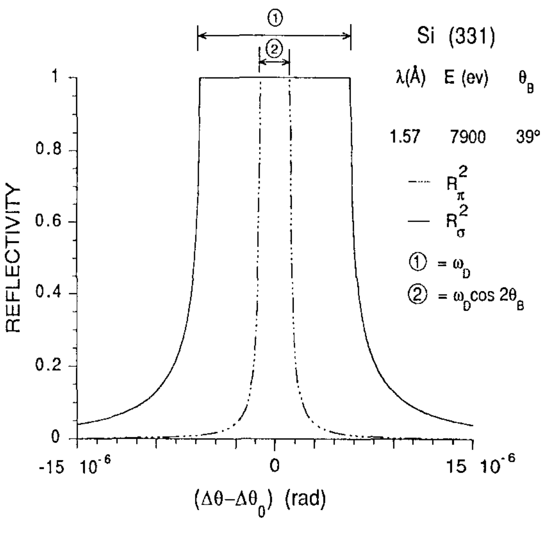

Fig. 4. Angular dependence of the σ (*solid line*) and π (*dashed-dotted line*) components reflectivities for two Si(331) symmetric reflections at $\lambda = 1.57$ Å. Case of non absorbing perfect crystals. Notice the smaller width of the π-component

$$\omega_D = \frac{2 r_e |F_{hkl}| \lambda^2}{\pi V \sin 2\theta_B}$$

C, the polarization factor, is equal to 1 for σ-polarization, and $\cos 2\theta_B$ for π-polarization. The integrated intensity, proportional to ω, becomes very small for π-polarization when the Bragg angle is nearly equal to 45°. If the monochromator is adjusted so that its plane of diffraction is perpendicular to the orbit plane (i.e. vertical), and the Bragg angle nearly equal to 45°, the polarization rate will be much increased.

Let us call $\tau_2 = \frac{I_\pi}{I_\sigma}$ the ratio of the integrated reflecting power of the π-component to that of the σ-component. The final ratio of the two components emerging from the monochromator after a double reflection is

$$\tau_f = \frac{N_\perp}{N_\parallel} \cdot \frac{I_\pi}{I_\sigma} = \tau_1 \cdot \tau_2$$

and the final polarization rate is equal to

$$P_f = \frac{1 - \tau_f}{1 + \tau_f} \tag{11}$$

Polarization by the Bragg Reflections: Case of Perfect Crystals With Absorption

In order to calculate τ_2 in a realistic case, that is in an absorbing case, it is necessary to recalculate for each reflection the integrated reflecting power of each component at the different wavelengths. For centrosymmetric crystals, and in the symmetric reflection geometry (Bragg case), the reflecting power of a single reflection R(y) is equal to (Carvalho 1986):

$$R(y) = L(y) - \sqrt{L(y)^2 - 1} \tag{12}$$

with

$$L = \frac{y^2 + z^2 + \sqrt{(y^2 - z^2 - 1 + x^2)^2 + 4(yz - x)^2}}{1 + x^2}$$

where

$$x = \frac{|\chi_{ih}|}{|\chi_{rh}|} \quad \text{and} \quad z = N \frac{\chi_{io}}{|C||\chi_{rh}|},$$

y is a parameter related to the departure from Bragg angle $\Delta\theta$ of the incident wave through

$$y = \frac{\Delta\theta \sin 2\theta + \chi_{r0}}{|C||\chi_{rh}|} = \frac{(\Delta\theta - \Delta\theta_0)\sin 2\theta}{|C||\chi_{rh}|},$$

$\underline{\chi}$ and $\underline{\chi}_i$ are respectively the real and imaginary parts of the electrical susceptibility and $\underline{\chi}_{rh}$ and $\underline{\chi}_{r0}$ (resp. $\underline{\chi}_{ih}$, $\underline{\chi}_{ih}$) their h and 0 Fourier components.

Figure 5 gives the theoretical reflectivies for σ and π components as a function of $(\Delta\theta - \Delta\theta_0)$ after two symmetric Si(331) reflections for θ equal to 39° and 46°. The integrated reflecting powers I_σ and I_π are then equal to:

$$I_\sigma = \int R_\sigma^2(y)\,dy \quad \text{and} \quad I_\pi = \int R_\pi^2(y)\,dy \tag{13}$$

and their ratio (τ_2) are reported in Table 1.

It will be now shown that a good approximation for these integrated reflecting powers is obtained using as an approximate function for R(y) a crenel function with a width equal to ω and an intensity equal to R(0) easily calculated from (12) (Fig. 6). With this approximation, I_σ and I_π are readily expressed as:

$$I_\pi(\theta_B) = \cos(2\theta_B)\,\omega_D R_\pi^2(0) \quad \text{and} \quad I_\sigma(\theta_B) = \omega_D R_\sigma^2(0). \tag{14}$$

Then τ_2 becomes equal to τ_2' and P_2 to P_2'

$$\tau_2' = \frac{R_\sigma^2(0)}{\cos 2\theta_B R_\pi^2(0)} \quad \text{and} \quad P_2' = \frac{1 - \tau_2'}{1 + \tau_2'} \tag{15}$$

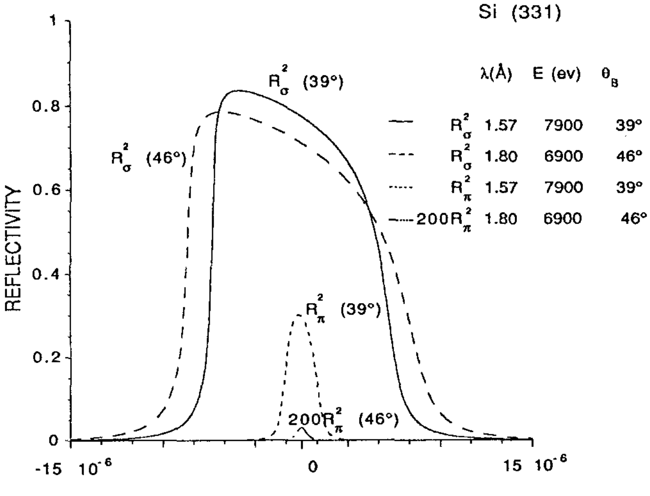

Fig. 5. Angular dependence of the σ and π components reflectivities for a double Bragg reflection at two wavelengths. Case of absorbing perfect crystals. The maximum value of the π-component vanishes when θ gets close to 45°

The values of $\underline{\tau}_2'$ are compared to those of $\underline{\tau}_2$ in Table 1. It can be seen that using $\underline{\tau}_2'$ instead of $\underline{\tau}_2$ gives the polarization rate with a good approximation since the difference between $\underline{P}_2$ and $\underline{P}_2'$ is less than 1.5% (Table 1). In the energy span of the EXAFS regime (6900–7900 eV), the Bragg angle of a Si(331) reflection is comprised between 39° and 46°. It comes out that the polarization rate introduced by a double reflection is greater than 85%. Finally, the full polarization rate $\underline{P}_f$ introduced by both the bending magnet and the monochromator varies between 99.40% and 100.00%.

Experimental

Sample

The mineral under study is a natural single crystal of diaspore (αAlOOH). It comes from the Mougla region (West Anatolia, Turkey). Its color is green, and its shape is prismatic (6 cm in length and about 2.5 cm in wide) with well developed (010), (100) and (110) faces parallel to the elongation axis $\underline{c}$. $\underline{a}$, $\underline{b}$ and $\underline{c}$ axes were determined by Laue diffraction, and confirmed on a $\theta/2\theta$ diffrractometer.

Table 1. Polarization rate by Bragg reflections for different wavelengths

λ	θ_B	τ_2	τ_2'	$P = \frac{1-\tau_2}{1+\tau_2}$	$P' = \frac{1-\tau_2'}{1+\tau_2'}$
0.85 Å	19.95°	7.5 10^{-1}	7.4 10^{-1}	14%	15%
1.57 Å	39.02°	7.2 10^{-2}	8.0 10^{-2}	87%	85%
1.75 Å	44.47°	1.5 10^{-6}	4.1 10^{-6}	100%	100%
1.80 Å	46.13°	2.4 10^{-4}	1.5 10^{-4}	100%	100%

τ_2 is the ratio of the integrated intensities without approximation
τ_2' is the ratio of the integrated intensities using the crenel approximate function for R

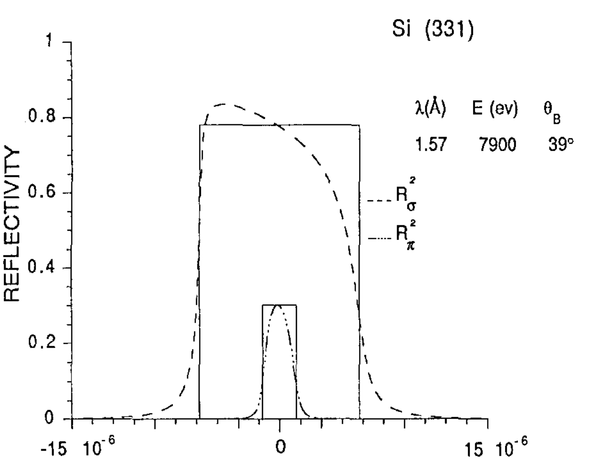

Fig. 6. Comparison between exact and approximate (*full line*) reflecting powers

The sample used in the EXAFS study was embedded in epoxy and prepared for electron microprobe analysis with an effective spot size estimated to be 10 μm. The wt% $Fe_2O_3/(Fe_2O_3+Al_2O_3)$ for 20 analyses ranged from 0.6 to 0.8% and no inclusion of a Fe-rich phase was detected at the micronic scale. The chemical formulae calculated from the chemical analyses and obtained by atomic absorption is: $Al_{0.9955}Fe_{0.0045}OOH$.

Data Collection

Experiments were performed at the French synchrotron radiation facility (LURE) using the EXAFS IV station. The DCI storage ring was operating at 1.85 GeV ($\underline{\lambda}_c = 3.4$ Å) and 250–300 mA. A double-crystal device (331) has been used to monochromatize the incident X-ray beam. Beam size at the sample was 3 mm high and 1 cm wide. Fe K-EXAFS spectra were collected ar room temperature in fluorescence mode using a scintillator plastic (Tourillon et al. 1990). A Mn filter was installed between the sample and the detector to remove unwanted elastically and inelastically scattered radiation. EXAFS spectra of the single crystal were recorded with the following orientations: $\underline{\varepsilon} \parallel [100]$, $\underline{\varepsilon} \parallel [010]$, and $\underline{\varepsilon} \parallel [001]$. The powder spectrum was collected at the magic angle (Manceau et al. 1990; Petiffer et al. 1990) to eliminate texture effects due to the needle shape of elementary crystallites. Bragg diffraction peaks were shifted out of the detector window by turning the monocrystal around an axis parallel to $\underline{\varepsilon}$. Depending on the orientation, the energy range of the data collection was between 6900–7900, 6900–7450, and 6900–7600 eV with 2 eV steps. Counting time per point was 5 seconds and spectra are the average of four to five scans.

Data Reduction

Data were analysed using the usual method of Fourier filtering; details on our data handling procedure have previously published (Manceau and Calas 1986). EXAFS contributions of nearest and next-nearest atomic shells have been filtered by a double Fourier transform. The first one, from the wavevector ($\underline{k}$) space to the real ($\underline{r}$) space yields a radial distribution function (RDF) uncorrected for phase functions, and has been performed using a Kaiser window (Bonnin et al. 1985; Manceau and Combes 1988). Structural parameters in terms of nature, number (N_j), and distance (r_j) of the filtered atomic shells were calculated by a least-squares fitting of the EXAFS contribution using empirical amplitude and phase functions. Lepidocrocite (γFeOOH) was used to extract empirical functions relative to the Fe–O and Fe–Fe atomic pairs. The empirical functions relative to the Fe–Al pair were calculated by interpolating the functions derived from $Mg(OH)_2$:Fe(Fe–Mg pair), and from biotite (Fe–Si atomic pair, Manceau et al. 1988).

Results

Powder EXAFS Spectrum

Its radial distribution function (RDF) displays two peaks centred at 1.3 Å and 2.7 Å (Fig. 7a). The former is attributed to the first oxygen atomic shell, and the latter to (Al, Fe) atomic neighbours. The Fourier filtered EXAFS contribution of the oxygen shell presents a wave-beating between 8.5–11 $Å^{-1}$, which indicates that Fe–O distances are incoherent (Fig. 8). This experimental contri-

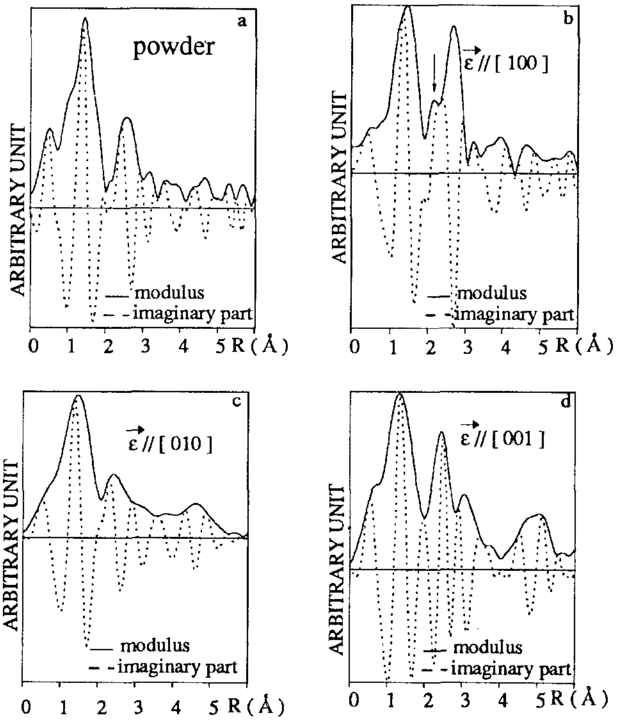

Fig. 7. Fe K radial distribution functions, uncorrected for phase functions, of diaspore powder **a** and single crystal: $\underline{\varepsilon} \parallel [100]$ **b**, $\underline{\varepsilon} \parallel [010]$ **c**, $\underline{\varepsilon} \parallel [001]$ **d**. The anisotropy of the local environment around Fe atoms is clearly visualized when comparing imaginary parts between 2 and 3.5 Å

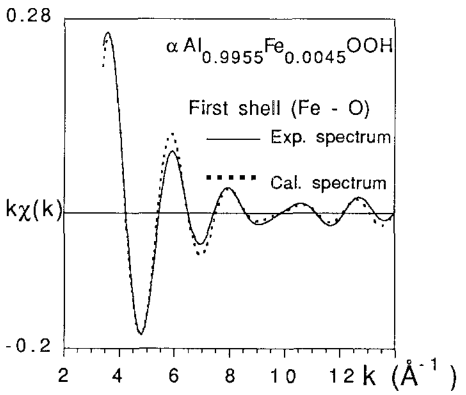

Fig. 8. Experimental and calculated kχ(k) EXAFS contribution of the first atomic shell (Fe–O) for diaspore powder. Notice the wave-beating between 8.5 and 11 $Å^{-1}$ indicative of a distribution of the Fe–O distances

bution can be nicely fitted assuming two oxygen subshells at 1.94 Å (3.2 neighbours) and 2.10 Å (2.6 neighbours). These bond lengths are characteristic of a Fe^{3+} ion in a 6-fold coordination. For instance, the EXAFS analysis of goethite (αFeOOH) realized using empirical functions extracted from lepidocrocite leads to 2.9 oxygens at 1.94 Å and 3.0 oxygens at 2.09 Å. If Fe atoms were divalent, Fe–O distances would have been of the order of 2.10–2.12 Å.

The second RDF peak is relatively broad. This suggests the presence of several cation shells. Figure 9a compares the contribution to EXAFS of these cation shells with a theoretical contribution where Fe atoms were supposed to be randomly substituted for Al. If so, Fe atoms would be surrounded by 2 Al at 2.92 Å + 2 Al at 3.19 Å + 4 Al at 3.37 Å (Table 2). This comparison results in a large phase mismatch over most of the k span. The result of this modeling is less than satisfactory. The obtention of a good spectral fitting can only be achieved assuming the presence of Fe neighbours in addition to Al ones. The assumption of only one Fe sub-shell at 3.01 Å, and one Al sub-shell at 2.97 Å results in a fairly good spectral fit (Fig. 9b). These two distances are characteristic of edge-sharing linkages (Table 2). Better fits can always be obtained by adding other cation contributions. But adjustable parameters increase in multishell fittings and their structural significance cannot be ascertained. Finally, analysis of the powder EXAFS spectrum leads to conclude that Fe^{3+} cations substitute for Al^{3+} in the diaspore lattice, and that they tend to cluster within octahedral chains.

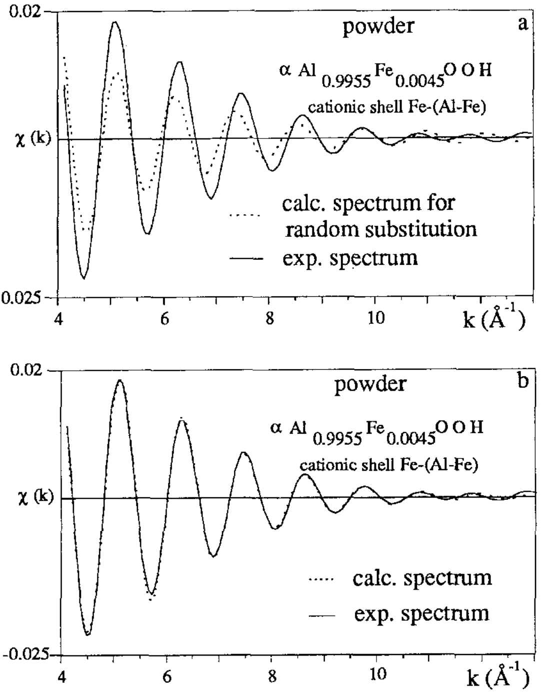

Fig. 9a, b. Fourier filtered χ(k) function of the two-nearest Me-contributions in the diaspore powder and fit. **a** Experimental curve (*solid line*) and modelisation (*dotted line*) for a random distribution of Fe atoms in the diaspore lattice. **b** Experimental curve (*solid line*) and modelisation with one Fe atom at 3.01 Å and one Al atom at 2.97 Å (*dotted line*)

Polarized EXAFS Spectra

P-EXAFS spectra for the three orientations are compared in Fig. 10. The angular dependence of χ is noteworthy, and indicates a strong structural anisotropy about Fe atoms. From these three independent measurements, the EXAFS spectrum of the powder has been calculated according to (8). It can be seen in Fig. 10d that the calculated spectrum matches well the experiment. In particular, the two shoulders between 4.5 and 5 Å^{-1} are fairly well reproduced even though this spectral shape could not be suspected when examining the three independent measurements. The mimesis between the experimental and the calculated powder spectra is particularly satisfying, and validates the reliability of our experimental work. More specifically, it credits the exactness in the orthogonality of orientations of the single crystal in the X-ray beam, and the elimination of texture effects in the powdered preparation at the magic angle.

The anisotropy of the local environment about Fe in diaspore is also clearly visualized when comparing the RDF derived from the three angular measurements (Fig. 7). The relative positions of the imaginary part of a Fourier transform formally depends on the nature of atoms in the shell under consideration. For two different shells at the same distance, the contrast in the relative positions is maximum when the difference of phase of their constituting atoms is π. Such a situation happens for Fe and (Al, Si) neighbours (Teo and Lee 1979) (Fig. 11). When applied to diaspore the foregoing discussion will permit to determine whether Fe atoms are predominantly surrounded by Al or Fe in each of the three lattice directions. From the examination of Fig. 7, it is concluded that Fe atoms have mainly Fe nearest neigh-

Table 2. Crystallographic data of reference compounds

Structure	Atomic pair	Face-sharing	sharing	Edge-sharing		Corner-	
		R(Å)	N	R(Å)	N	R(Å)	N
γFeOOH lepidocrocite	Fe–Fe	– –	– –	3.054 3.06	4 2	3.87	2
βFeOOH akaganeite	Fe–Fe	–	–	3.01 3.075	2 2	3.66	4
αAlOOH diaspore	Al–Al	–	–	2.845 3.10	2 2	3.29	4
αFeOOH goethite	Fe–Fe	–	–	3.01 3.28	2 2	3.46	4
α(Al, Fe)OOH ramdon distribution	Fe–Al	–	–	2.92 3.19	2 2	3.37	4
αAl_2O_3 corundum	Al–Al	2.65	1	2.79	3	3.22	3
αFe_2O_3 hematite	Fe–Fe	2.89	1	2.97	3	3.37 3.70	3 6
$\alpha(Al, Fe)_2O_3$ random distribution	Fe–Al	2.77	1	2.88	3	3.295	3

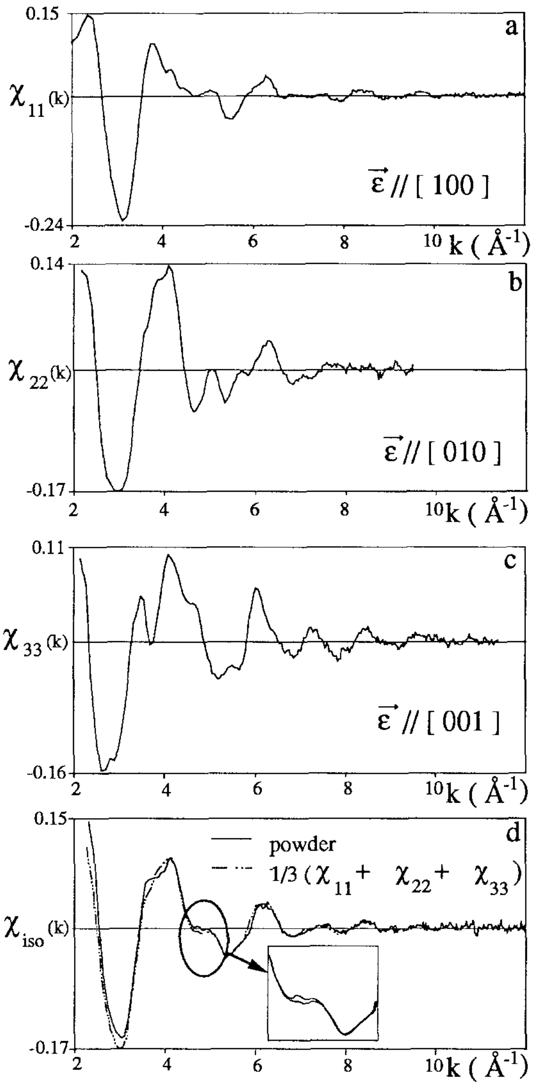

Fig. 10a–d. P-EXAFS spectra of the diaspore single crystal. **a** $\varepsilon \parallel [100]$; **b** $\varepsilon \parallel [010]$; **c** $\varepsilon \parallel [001]$. **d** comparison between the isotropic spectrum, calculated from the three single crystal measurements between 2.5 and 9.5 Å^{-1}, and the experimental powder spectrum collected at the magic angle

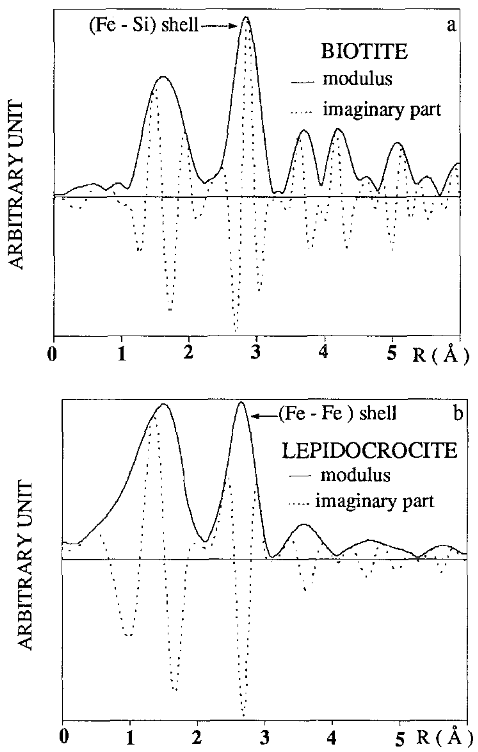

Fig. 11. Fe K radial distribution functions, uncorrected for phase functions, of biotite ($\varepsilon \parallel [001]^*$) and lepidocrocite (powder spectrum). Imaginary parts of the Fe–Fe and Fe–(Si, Al) pairs are out of phase

bours in the a and b directions, and Al nearest neighbours in the c direction.

This first qualitative result confirms that Fe atoms are not diluted into the diaspore framework, but tend rather to segregate. But going further in the analysis of RDF, the presence of a Fe peak centred at short distance in the $\varepsilon \parallel [010]$ direction is unexpected inasmuch as the nearest metal contribution in the direction of channels should be at about 3.19 Å (Table 3). Fit of this contribution yields 2.7 Fe at 2.89 Å and 4.8 Al at 3.19 Å (Table 3). Likewise, in the $\varepsilon \parallel [100]$ direction the presence of a small bump on the left-side of the first Fe–Me RDF peak (see arrow) suggests the presence of nearest Fe or Al neighbours at a short distance. In order to avoid loss of information during data reduction, Fourier back transformation was carried out over the range 1.9–3.2 Å, which contains contributions of the two nearest (Al, Fe) shells. Least-squares modeling of these back transformed EXAFS functions yields 2.5 Al at 2.70 Å and 3.0 Fe at 3.07 Å. The short Fe–Fe and Fe–Al distances at 2.89 Å and 2.70 Å, respectively, are worth mentioning as none of these are expected in an α(Al, Fe)OOH structure. These clearly indicate that Fe atoms are not simply clustered within the diaspore lattice.

Discussion

The Polyhedral Approach

In solids Me–Me distances formally depend on the way by which polyhedra are linked one to another. For example, in Fe^{3+} oxides the $Fe^{3+}-Fe^{3+}$ distances across one octahedral face (F linkage), one edge (E linkage), two corners (double-corner, DC linkage), and one corner (single-corner, SC linkage), are equal to about 2.89 Å, 2.97–3.075 Å (with an additional distance at 3.28 Å in αFeOOH), 3.37–3.7 Å, and 3.9 Å, respectively (Table 2, Fig. 12, and Manceau and Combes 1988). Likewise, in αAl_2O_3 and αAlOOH, the Al–Al distances across a face, an edge and two corners are equal to 2.65 Å, 2.79–3.10 Å and 3.22–3.29 Å, respectively (Table 2). It result that from the knowledge of the number and distance of the two- or three-nearest cations it is possible to model the way by which octahedra are joined to each other. The validity of such a *polyhedral approach* has been tested onto well-crystallized FeOOH (Fig. 12), and MnO_2 polymorphs (Manceau and Combes 1988), and, ever since,

Table 3. EXAFS data and models of Fe clusters [σ(Å) is the EXAFS Debye-Waller factors]

Local structure around Fe atoms	Direction	Atomic pair	Face-sharing				Edge-sharing				Corner-sharing			
			R_j(Å)	N_j	θ_j	σ(Å)	R_j(Å)	N_j	θ_j	σ(Å)	R_j(Å)	N_j	θ_j	σ(Å)
EXAFS data	$\varepsilon \parallel [001]$	Fe–Al	–	–	–	–	2.88	5.0	–	0.01	–	–	–	–
		Fe–Fe	–	–	–	–	3.00	1.3	–	0.02	–	–	–	–
	$\varepsilon \parallel [010]$	Fe–Al	–	–	–	–	3.19	4.8	–	0.00	–	–	–	–
		Fe–Fe	2.89	2.7	–	0.03	–	–	–	–	–	–	–	–
	$\varepsilon \parallel [100]$	Fe–Al	2.70	2.5	–	0.02	–	–	–	–	–	–	–	–
		Fe–Fe	–	–	–	–	3.07	3.0	–	0.03	–	–	–	–
Models														
α(Al, Fe)OOH	$\varepsilon \parallel [001]$	Fe–Al	–	–	–	–	2.92	6.0	0.0°	–	3.37	2.30	64.2°	–
		Fe–Al	–	–	–	–	3.19	1.3	62.6°	–	–	–	–	–
	$\varepsilon \parallel [010]$	Fe–Al	–	–	–	–	2.92	0.0	90.0°	–	3.37	4.40	53.0°	–
		Fe–Al	–	–	–	–	3.19	4.6	27.4°	–	–	–	–	–
	$\varepsilon \parallel [100]$	Fe–Al	–	–	–	–	2.92	0.0	90.0°	–	3.37	5.30	48.2°	–
		Fe–Al	–	–	–	–	3.19	0.1	83.0°	–	–	–	–	–
α(Al, Fe)$_2$O$_3$ (3 Fe octahedra)	$\varepsilon \parallel [001]$	Fe–Al	–	–	–	–	2.92	4.0	–	–	–	–	–	–
		Fe–Al	–	–	–	–	2.97	0.8	–	–	3.37	1.1	–	–
		Fe–Fe	–	–	–	–	2.97	0.5	–	–	3.37	0.4	–	–
		Fe–Al	–	–	–	–	3.19	0.8	–	–	–	–	–	–
	$\varepsilon \parallel [010]$	Fe–Fe	–	–	–	–	2.89	2.0	–	–	–	–	–	–
		Fe–Fe	–	–	–	–	2.97	0.1	–	–	3.37	0.7	–	–
		Fe–Al	–	–	–	–	2.97	0.3	–	–	3.37	2.2	–	–
		Fe–Al	–	–	–	–	3.19	3.0	–	–	–	–	–	–
	$\varepsilon \parallel [100]$	Fe–Fe	–	–	–	–	2.97	1.3	–	–	3.37	0.9	–	–
		Fe–Al	–	–	–	–	2.97	1.9	–	–	3.37	2.7	–	–
α(Al, Fe)$_2$O$_3$ (4 Fe octahedra)	$\varepsilon \parallel [001]$	Fe–Al	–	–	–	–	2.92	4.5	–	–	–	–	–	–
		Fe–Al	–	–	–	–	2.97	0.4	–	–	3.37	1.1	–	–
		Fe–Fe	–	–	–	–	2.97	0.4	–	–	3.37	0.6	–	–
		Fe–Al	–	–	–	–	3.19	0.9	–	–	–	–	–	–
	$\varepsilon \parallel [010]$	Fe–Fe	–	–	–	–	2.89	1.5	–	–	–	–	–	–
		Fe–Fe	–	–	–	–	2.97	0.2	–	–	3.37	1.0	–	–
		Fe–Al	–	–	–	–	2.97	0.2	–	–	3.37	2.2	–	–
		Fe–Al	–	–	–	–	3.19	3.5	–	–	–	–	–	–
	$\varepsilon \parallel [100]$	Fe–Fe	–	–	–	–	2.97	1.9	–	–	3.37	1.3	–	–
		Fe–Al	–	–	–	–	2.97	1.4	–	–	3.37	2.7	–	–

has been successfully applied to the determination of the local structure of a number of disordered hydrous Fe oxides, and to mineral-surface geochemistry (see e.g. Combes et al. 1989, 1990; Manceau et al. 1992; Charlet and Manceau 1991). However, in the case of heterocationic oxides the extension of the polyhedral approach from known to unknown structures is no longer straightforward, and need to be discussed before being applied to this α($Al_{0.9955}Fe_{0.0045}$)OOH sample. Two cases must be considered as to whether Fe octahedra are linked to each other, or linked to Al octahedra.

In the former situation, one may consider that, at the local scale, the αAlOOH lattice is relaxed, and that Fe–Fe distances found in Fe^{3+} oxides are roughly preserved in the aluminous framework. Evidences of local relaxations in solid-solutions are numerous as long as one is just considering the first coordination sphere of cations (Boyce and Mikkelsen 1989), and are readily explained by the Pauling's concept of the conservation of atomic radii. But, eventhough relaxation effects cannot be strictly extended to interpolyhedral bond angles, given the very small Fe concentration, Fe–Fe distances in the αAlOOH lattice are most probably very close to the ones in Fe oxides. In the latter topological association, i.e. whenever a Fe(O, OH)$_6$ octahedron is linked to a Al(O, OH)$_6$ octahedron, Fe–Al distances shall also depend on the way octahedra are joined to each other. For each of octahedral associations these distances are estimated to be equal to half the Fe–Fe and Al–Al values (Table 2).

Local Structure of Fe Clusters

The first model one might think of is the existence of goethite clusters within the diaspore framework. This model is consistent with results obtained in the c direction as the existence of 1.3 Fe at 3.00 Å and 5 Al at 2.88 Å is readily attributed to the nearest cation shell across edges of a single α(Al, Fe)OOH octahedral chain

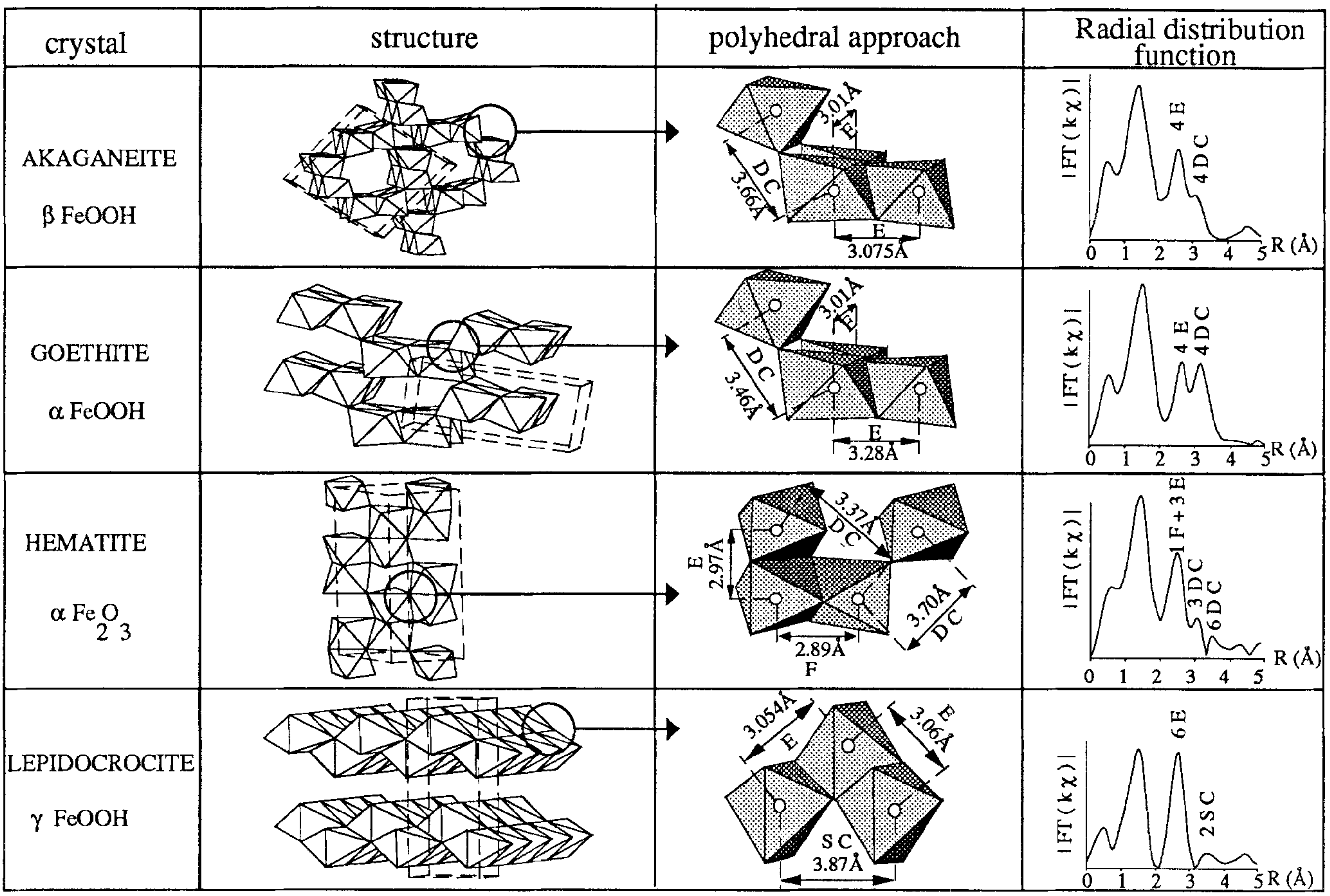

Fig. 12. Polyhedral approach of the structure of Fe-oxides. The structure of α-, β-, γ-FeOOH and α-Fe_2O_3 can be differentiated at the local scale by EXAFS owing to their distinct octahedral linkages and/or Fe—Fe distances

(Table 3). However, this model is not tenable with regard to results in the two other directions. First, in the a direction, the shortest Me atomic shell should be at 3.37 Å (Al neighbours) or 3.46 Å (Fe neighbours). Second, it does not account for Fe—Fe pairs at 2.89 Å (b direction) and Fe—Al pairs at 2.70 Å (a direction). These two distances well match with a face linkage between two Fe octahedra, and between Fe and Al octahedra, respectively (Table 2). Therefore, whereas some Fe atoms of a cluster substitute for Al in octahedral chains, these ones, or others, have nearest Fe and Al neighbours across faces in the directions of tunnels.

The simplest structural model, which can then be hypothesized, is a cluster of three Fe octahedra, one of these being located in the tunnel, and the two other belonging to two different chains (Fig. 13). In this model, interoctahedral $Fe(O, OH)_6$ linkages are identical to those found in hematite (Fig. 12). The insertion of small hematite-like clusters into the diaspore structure is geometrically easily feasible, suffice to place a Fe atom into a tunnel at a position (0a, 0.3b, 0c) from the nearest Fe pointing in b direction (Fig. 13). The mean Fe—Fe and Fe—Al distances and number of cation neighbours of such a cluster are reported in Table 4. Keeping in mind that, first, the difference of phase between Fe and Al is close to π, second, the contribution to EXAFS of a Fe neighbour is about twice as intense as that of an

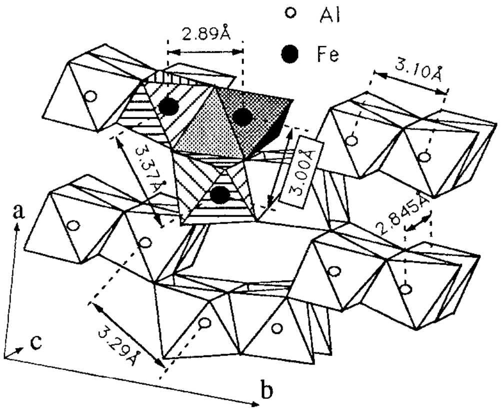

Fig. 13. Structural model of the natural Fe-containing diaspore. Fe atoms are segregated within the diaspore framework, and build hematite-like clusters in the [010] direction of channels. The face-sharing of tunnel Fe octahedra with Al octahedra has not been pictured

Al neighbour, this cluster should provide the following EXAFS results: $\varepsilon \parallel [001]$: 4 Al at 2.92 Å + δNFe at 2.97 Å; $\varepsilon \parallel [010]$: 2 Fe at 2.89 Å + 3 Al at 3.19 Å; $\varepsilon \parallel [100]$: δNFe at 2.97 Å (Table 3). With the exception of the Fe—Al atomic pair at 2.70 Å in the a direction, which is not accounted for by this model, it integrates all the other experimental data. The Fe—Al contribution at 2.70 Å corresponds to the presence in channels of Fe octahedra linked to the borders of aluminous chains by sharing a face. These Fe octahedra can either be isolated, or can belong to the aforedescribed Fe cluster. Indeed it cannot be ruled out that a given channel Fe octahedron might share two faces with octahedra of two different chains, i.e. with a Fe octahedron in the b direction plus an Al octahedron in the c direction. The average number of cations around Fe has also been calculated assuming a cluster made up by 4 octahedra. It is seen in Table 3 that there is only a weak sensitivity of the average Fe local environment to the cluster size. But eventhough EXAFS spectroscopy fails to determine the average size of the Fe clusters, given the very small concentration of Fe atoms and the good crystallinity of this single crystal of diaspore, the existence of large Fe domains is unlikely.

Finally, the average structure of the Fe clusters can be simply modeled as follows (Fig. 13). They consist of small hematite units as the one pictured in Fig. 12. Each of these clusters is topotactically grafted to one aluminous double-chain by edge-sharings (d[Fe – Al = 2.88 Å and 3.19 Å), and, may-be, to a nearby second aluminous double chain by a face-sharing (d[Fe – Al] = 2.70 Å). The only certainty concerning the topological relationships entertained by Fe octahedra located in tunnels is that they share a face with a Fe octahedron in the b direction and/or with an Al octahedron in the a direction. Banfield and Velben (1991) have recently identified hematite platelets in the (001) plane of rutile, a mineral which also possesses a channel structure along a axis. The close structural likeness between Fe-containing rutile and diaspore provides additional support on the validity of the proposed model.

Formation Process of Fe Clusters

Two mechanisms are possible: (1) a surface precipitation of hematite-like clusters during the growth of diaspore or (2) a diffusion of Fe and ultimate precipitation within the diaspore framework. Diaspore generally forms in non, or slightly, metamorphic conditions. Natural occurrence of diaspore pledges in favour of a surface precipitation mechanism.

Thus, Fe clusters are viewed as αFe_2O_3 nuclei formed by an heterogeneous nucleation onto an $\alpha AlOOH$ substratum. These two structures consist of an hexagonal oxygen close packing, they only differ by the ordering of Me atoms in octahedral sites. On a topological point of view, both diaspore and hematite have edge and corner linkages, but hematite has in addition face linkages. This structural mimesis, as well as the similarity of Fe^{3+} and Al^{3+} ionic radii, renders feasible the topotactic growth of hematite onto diaspore.

The formation process of these Fe clusters can be understood at the light of the recent investigation, at a molecular level, of the heterogeneous nucleation and the further crystal growth of $\gamma CrOOH$ onto $\alpha FeOOH$ (Charlet and Manceau 1991). It has been shown that $\gamma CrOOH$-like multinuclear surface complexes can form in conditions largely undersaturated with respect to the homogeneous precipitation, and even when Cr atoms are bonding only 10% of reactive surface sites. Cr atoms were found in a mixed $\alpha(Fe, Cr)OOH - \gamma(Fe, Cr)OOH$ local environment. At larger Cr concentration, once full surface coverage was reached, a 3D phase started growing, whose structure was different from the substratum one ($\alpha FeOOH$), but similar to that of the surface complexes ($\gamma CrOOH$), which acted therefore as precipitation nuclei. In the present study, Fe atoms are in a mixed $\alpha(Al, Fe)OOH - \alpha(Al, Fe)_2O_3$ microstructure, and one may assume that a 3D hematite lattice would have grown if the activity of Fe in solution, at the time of the cluster nucleation, had been high enough.

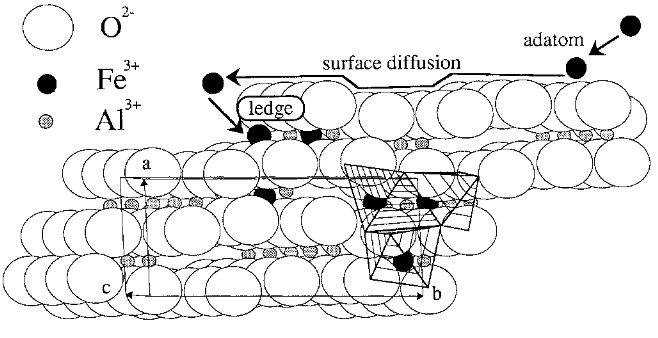

Fig. 14. Mechanistic interpretation of the formation of hematite-like surface complexes at the time of the diaspore growth

Monte Carlo simulations of crystal growth (Lasaga 1990) and dissolution (Wehrli 1989a, 1989b) kinetics have now well shown that surface sites of solids have different activation energies, and that the greater the number of sorbate-sorbent bondings, the less reactive (i.e. the more stable) the surface site. Using this theoretical framework, the scenario of formation of Fe complexes can be mechanistically described at the molecular-level as follows (Fig. 14). In a first stage, Fe^{3+} ions sorb at the surface of the growing diaspore. These adatoms diffuse in surface until reaching a thermodynamically stable position, i.e. like do Al^{3+} ions. But, in addition, sorbed Fe atoms tend to segregate at the sorbent surface, and to share edges and corners like in $\alpha(Al, Fe)OOH$. Further on, new sorbed Fe^{3+} ions will diffuse towards pre-existent "$\alpha FeOOH$ surface clusters" to join them through face- and edge-sharings realizing, at the local scale, an "αFe_2O_3 cluster". If this newly sorbed Fe octahedron also shares a face with a nearby Al octahedron, then Fe atoms belonging to a surface complex will possess a mixed $\alpha(Al, Fe)OOH$ a, b and c directions) – αFe_2O_3 (b direction) – $\alpha(Al, Fe)_2O_3$ (a direction) local structure. Otherwise, some Fe atoms will have a mixed $\alpha(Al, Fe)OOH - \alpha Fe_2O_3$ local structure, and the others a mixed $\alpha(Al, Fe)OOH - \alpha(Al, Fe)_2O_3$ local structure as to whether the Fe octahedron sorbed in a channel shares a face with a Fe or an Al octahedron. This atomic scenario is conceptually very close to the "surface precipitation model" developed by Farley et al. (1985), and which interprets adsorption phenomena as a continuum between specific adsorption and surface precipitation. At present this model had been validated at the microscopic level by only few works (Murray and McBride 1978; Davis et al. 1987; Wersin et al. 1990; Charlet and Manceau 1991); however none of these studies has been able to describe the 3D local structure of these multinuclear surface complexes. Owing to the gain in accuracy of the structural analysis achieved by polarized EXAFS, this first advanced structural description of a surface complex allows us to make inroads towards a much better understanding of sorption phenomena at the atomic level.

Conclusion

This study represents the first detailed 3D local structural description of a cluster of heteroatoms in a mineral. This break-through has been possible owing to the gain in structural precision generated by angular measurements of EXAFS spectra. It is shown that this cluster possesses an hematite-like local structure, and is topotactically bound to the diaspore lattice. This cluster is thought to correspond to an ancient surface complex, which has formed at the time of the diaspore growth, and which is now sealed within its bulk structure. As a matter of fact, the whole crystal of diaspore has kept the memory of the surface precipitation mechanism of the ancient surface complex, i.e. heterogeneous nucleation. Together with the recognition by Boudeulle and Muller (1988) of epitaxial growths of hematite and goethite crystals onto kaolinite, from now on, there is a growing awareness that, in the physico-chemical conditions of the earth's surface, heterogeneous nucleation is the rule rather than the exception. Besides, several spectroscopic studies have revealed that materials formed in these conditions are chemically and structurally extremely heterogeneous at the local scale, and that their local structure is often different from the averaged, diffraction-based, structure (Muller et al. 1992). These findings have led to the conclusion that low temperature solids rarely crystallize according to equilibrium thermodynamics. In addition to the well-known examples of atom segregations, ion vacancies, and intergrowths of discrete phases, this new type of crystal defect represents an other evidence of non-equilibrium process.

A good knowledge of the actual crystallographic location of trace elements in natural samples is also essential to valid laboratory investigations of sorption reaction mechanisms at the mineral/water interface. For instance, several of these studies have shown that hydrolysable cations tend also to form multinuclear surface complexes when chemisorbed on mineral surfaces (Tewari and Lee 1975; Bleam and McBride 1985; Motschi 1987; Wersin et al. 1990; Chisholms-Brause et al. 1990a, 1990b; Charlet and Manceau 1991). As a consequence, on going spectroscopic studies of natural and synthetic systems have demonstrated their capacity to shed direct light on elementary mineral surface reactions, which control the geochemical behaviour of elements, and in turn, the precipitation and dissolution of solids.

Acknowledgement. Authors have pleasure to thank the staff of LURE for the synchrotron facility.

References

Banfield JF, Veblen DR (1991) The structure and origin of Fe-bearing platelets in metamorphic rutile. Amer Mineral 76:113–127

Bleam WF, McBride MB (1985) Cluster formation versus isolated-site adsorption. A study of Mn(II) and Mg(II) adsorption on boehmite and goethite. J Colloid Interface Sci 103:124–132

Bonnin D, Calas G, Suquet H, Pezerat H (1985) Sites occupancy of Fe^{3+} in Garfield nontronite: a spectroscopic study. Phys Chem Minerals 12:55–64

Boudeulle M, Muller JP (1988) Structural relationships with kaolinite in a laterite from Cameroon. A TEM study. Bull Miner 111:149–166

Boyce JB, Mikkelsen JC (1989) Local structure of pseudobinary semiconductor alloys: An X-ray absorption fine structure study. J Cryst Growth 98:37–43

Brouder C (1990) Angular dependence of X-ray absorption spectra. J Phys 2:701–738

Carvalho C (1986) Thesis. University of Sao Paulo, Brazil

Charlet L, Manceau A (1991) X-ray absorption spectroscopic study of the sorption of Cr(III) at the oxide/water interface. II Adsorption, coprecipitation and surface precipitation on ferric hydrous oxides. J Colloid Interface Sci (in press)

Chisholms-Brause CJ, Hayes KF, Roe AL, Brown GE Jr, Parks GA, Leckie JO (1990a) Spectroscopic investigation of Pb(II) complexes at the γ-Al_2O_3/water interface. Geochim Cosmochim Acta 7:1897–1909

Chisholms-Brause CJ, O'Day PA, Brown GE Jr, Parks GA (1990b) Evidence for multinuclear metal-ion complexes at the solid/water interfaces from X-ray adsorption spectroscopy. Nature 348:528–530

Chuchrov FV, Gorshkov AI, Vitovskaya IV, Drits VA, Sivtsov AV, Rudnitskaya YS (1980) Crystallochemical nature of Co – Ni asbolane. An SSSR Izvestiya, Ser Geol 6:73–81. (Trans Internat Geol Rev 24, 5, 346–354)

Chuchrov FV, Gorshkov AI, Drits VA (1987) News in Crystallochemistry of manganese hydroxides. Zapiski Vsesoyusnogo Mineralogicheskaya Obchestva CXVI:210–222

Combes JM, Manceau A, Calas G, Bottero JY (1989) Formation of ferric oxides from aqueous solutions: a polyhedral approach by X-ray absorption spectroscopy. I. Hydrolysis and formation of ferric gels. Geochim Cosmochim Acta 53:583–594

Combes JM, Manceau A, Calas G (1990) Formation of ferric oxides from aqueous solutions: a polyhedral approach by X-ray absorption spectroscopy. II. Hematite formation from ferric gels. Geochim Cosmochim Acta 54:1083–1091

Davis JA, Fuller CC, Cook AD (1987) A model for trace metal sorption processes at the calcite surface: Adsorption of Cd^{2+} and subsequent solid solution formation. Geochim Cosmochim Acta 51:1477–1490

Farley KJ, Dzombak DA, Morel FMM (1985) A surface precipitation model for the sorption of cations on metal oxides. J Colloid Interface Sci 106:226–242

Goodkoep JB (1989) X-ray dichroism of rare earth materials. Thesis. University of Nijmegen, Holland

Lasaga AC (1990) Atomic Treatment of mineral water Surface Reactions. In: Hochella MF, Art FW (eds) Mineral-water interface geochemistry. Rev Mineral 23:17–86

Manceau A, Calas G (1986) Nickel-bearing clay minerals: 2. intracrystalline distribution of nickel: An X-ray absorption study. Clay Miner 15:341–360

Manceau A, Llorca S, Calas G (1987) Crystal chemistry of cobalt and nickel in lithiophorite and asbolane from New Caledonia. Geochim Cosmochim Acta 51:105–113

Manceau A, Combes JM (1988) Structure of Mn and Fe oxides and oxyhydroxides: a topological approach by EXAFS. Phys Chem Minerals 15:283–295

Manceau A, Decarreau A (1988) Extended X-ray absorption fine structure study of cobalt-exchanged sepiolite: a comment on the paper by Fukushima and Okamoto. Clay Miner 36:382–383

Manceau A, Bonnin D, Kaiser P, Frétigny C (1988) Polarized EXAFS of biotite and chlorite. Phys Chem Minerals 16:180–185

Manceau A (1990) Distribution of cations among the octahedra of phyllosilicates: insight from EXAFS. Can Miner 28:321–328

Manceau A, Bonnin D, Stone WE, Sanz J (1990) Distribution of Fe in the octahedral sheet of trioctahedral micas by polarized EXAFS. Comparison with NMR results. Phys Chem Minerals 17:363–370

Manceau A, Gorshkov AI, Drits VA (1992) Structural chemistry of Mn, Fe, Co and Ni in Mn hydrous oxides. II Information from EXAFS spectroscopy, electron and X-ray diffraction. Am Miner (submitted)

Motschi H (1987) Aspects of the molecular structure in surface complexes: spectroscopic investigations. In: Stumm W (ed) Aquatic Surface Chemistry. Wiley, New York, pp 11–126

Müller JE, Wilkins JW (1984) Band structure approach to the X-ray spectra of metals. Phys Rev B 29:4431–4348

Muller JP, Calas G, Manceau A, Clozel B, Hazemann JL, Ildefonse P (1992) Crystal chemistry of claxs and associated oxides: constraints for modelling element transfer at the Earth's surface. Chem Geol (submitted)

Murray B, McBride MB (1978) Retention of Cu^{2+}, Ca^{2+}, Mg^{2+} and Mn^{2+} by amorphous Alumina. Soil Sci Soc Am J 42:27–31

Parrat LG (1954) Surface studies of solids by total reflection of X-ray. Phys. Rev 95:359–369

Petiffer RF, Brouder C, Benfatto M, Natoli CR, Hermes C, Ruis Lopez MF (1990) Magic angle theorem in powder X-ray absorption spectroscopy. Phys Rev B42:37–42

Schulze DG (1984) The influence of aluminium on iron oxides. VIII: Unit-cell dimensions of Al-substituted goethites and estimation of Al from them. Clay Miner 32:36–44

Schulze DG, Schwertmann U (1984) The influence of aluminium on iron oxides. X. Properties of Al-substituted goethites. Clay Miner 19:521–529

Schulze DG, Schwertmann U (1987) The influence of aluminium on iron oxides. XIII. Properties of goethites synthesized in 0.3 KOH at 25°. Clay Miner 22:83–92

Stern EA, Heald SM (1983) Basic principles and applications of EXAFS. In: Koch E (ed) Handbook on Synchrotron Radiation. North Holland, Amsterdam New York, pp 955–1014

Tafto J, Buseck PR (1983) Quantitative study of Al–Si ordering in an orthoclase feldspar using an analytical transmission electron microscope. Am Miner 68:944–950

Tewari PH, Lee W (1975) Adsorption of Co(II) at the oxide-water interface. J Colloid Interface Sci 52:77–88

Thiel R (1963) Zum System $\alpha-\mathrm{FeOOH}-\alpha-\mathrm{AlOOH}$. Z Anorg Allg Chem 326:70–77

Teo BK, Lee PA (1979) Ab initio calculations of amplitude and phase functions for extended X-ray absorption fine structure spectroscopy. Am Chem Soc 101:2815–2832

Tourillon G, Guay D, Lemonier M, Bartol F, Badeyan M (1990) X-Ray Absorption spectroscopy: A fluorescence detection system based on a plastic scintillator. Nucl Instrum Methods A294:382–390

Vvedensky DD, Pendry JB, Döbler V, Baberschke K (1987) Quantitative multiple-scattering analysis of near-edge X-ray absorption fine structure: $C(2*2)O$ on Cu(100). Phys Rev B35:7756–7759

Waychunas GA, Brown GE (1990) Polarized X-ray absorption spectroscopy of Metal ions in Minerals: Applications to site Geometry and electronic structure determination. Phys Chem Minerals 17:420–430

Wehrli B (1989a) A Monte Carlo simulations of surface morphologies during mineral dissolution. J Colloid Interface Sci 132:230–242

Wehrli B (1989b) Surface structure and mineral dissolution Kinetics: a Monte Carlo study. In: Miles DL (ed), Water-rock Interaction. Bolkema AA, Rotterdam, pp 751–753

Wersin P, Charlet L, Karthein R, Stumm W (1990) From adsorption to precipitation: Sorption of Mn^{2+} on $FeCO_3$(s). Geochim Cosmochim Acta 53:2787–2796

Wuilleumier F (1973) Le rayonnement synchrotron émis par les anneaux de stockage d'Orsay (ACO et DCI). Rapport interne du Laboratoire pour l'Utilisation du Rayonnement Electromagnetique (LURE) Orsay France

Zachariasen WH (1945) "Theory of X-ray Diffraction in crystals." Wiley, New York